Journal of Alloys and Compounds 1057 (2026) 186787

Contents lists available at ScienceDirect

Journal of Alloys and Compounds

journal homepage: www.elsevier.com/locate/jalcom

Insights into the compatibility of a metastable FeMnCoCr high entropy alloy with a Fe-based shape memory alloy

J.G. Lopes [a,*], A. Alvarez [a], J. Shen [a], T. Boll [b], D. Wang [b], B. Li [c,d], B. Wang [c,d], N. Schell [e], R.S. Mishra [f,g], A.C. Baptista [a], J.P. Oliveira [a]

[a] CENIMAT/I3N, Department of Materials Science, NOVA School of Science and Technology, Universidade NOVA de Lisboa, Caparica 2829-516, Portugal
[b] Karlsruhe Nano Micro Facility (KNMF), Institute for Applied Materials (IAM-WK), Institute for Nanotechnology (INT), Karlsruhe Institute of Technology (KIT), Hermann-von-Helmholtz-Platz 1, Eggenstein-Leopoldshafen 76344, Germany
[c] Western Superconducting Technologies Co., Ltd., Shaanxi Province Engineering Laboratory for Aerial Material, Xi'an 710018, China
[d] National Key Laboratory for Precision Hot Processing of Metals, School of Materials Science and Engineering, Harbin Institute of Technology, Harbin 150001, China
[e] Institute of Materials Physics, Helmholtz-Zentrum Hereon, Max-Planck-Str. 1, Geesthacht 21502, Germany
[f] Center for Friction Stir Processing, Department of Materials Science and Engineering, University of North Texas, Denton, TX 76207, USA
[g] Advanced Materials and Manufacturing Processes Institute, University of North Texas, Denton, TX 76207, USA

ARTICLE INFO

Keywords:
High entropy alloys
Shape memory alloy: Gas tungsten arc welding
Synchrotron X-ray diffraction
Atom probe tomography
Microstructure
Mechanical testing

ABSTRACT

High entropy alloys (HEA) are novel advanced materials that have been subjected to extensive research due to their outstanding properties and potential for key engineering applications. Given this, research on their processability must be conducted to avoid premature failure during operation. Gas tungsten arc welding is a widely available technology capable of generating high performing and permanent joints. Furthermore, within this technology, dissimilar welding is a relevant topic given the frequent necessity to join different materials, allowing for greater design freedom while decreasing material costs. In this study, dissimilar welding of a FeMnCoCr HEA with a Fe-based shape memory alloy was conducted, allowing an inquiry into the compatibility between the two advanced engineering alloys. By employing both conventional and advanced characterization techniques, including optical and electron microscopy, atom probe tomography and synchrotron x-ray diffraction, a comprehensive understanding of the effect of processing condition on the microstructure and mechanical response of the joints is obtained. With this work we intend to highlight a pathway for the introduction of HEAs in modern day engineering industry.

1. Introduction

Within the scope of studying novel advanced materials for key engineering applications, high entropy alloys (HEA) stand in the vanguard of possibilities to achieve high performing solutions. At this moment, this novel class of materials comprises numerous systems, which can exhibit a plethora of different properties depending on the elements that compose it.

According to the first insights on HEAs in the literature [1,2], such multi-element compositions confer these materials four distinct core effects. These are the "high entropy effect", the "lattice distortion effect", the "sluggish diffusion effect" and the "cocktail effect". Where the high entropy effect favors solid solutions over intermetallic compounds, while the lattice distortion stems from different atoms of different sizes occupying the lattice positions of a crystal structure, promoting its distortion. Additionally, sluggish diffusion constrains the atomic diffusion of the elements and inhibits the phase transformations, and the cocktail effect refers to the enhancement of the established properties of the alloy, which cannot be attributed independently to any of the elements.

However, the field of HEAs has progressed substantially since its inception. Nowadays, it is possible to design and optimize HEAs with focus in a range of properties, rather than aiming to achieve a single-phase HEA with established properties [3,4]. For instance, improved wear resistance can be achieved through dynamic surface segregation [5,6], while enhanced oxidation resistance has been associated with the high activation energy of atomic diffusion in these alloys, resulting in a reduced rate of penetration of the corrosive medium into the material

* Corresponding author.
E-mail addresses: jcg.lopes@fct.unl.pt, jp.oliveira@fct.unl.pt (J.G. Lopes).

https://doi.org/10.1016/j.jallcom.2026.186787
Received 28 December 2025; Received in revised form 31 January 2026; Accepted 10 February 2026
Available online 14 February 2026

[7,8]. In addition, irradiation tolerance in refractory HEAs is improved as irradiation-induced grain boundary embrittlement is significantly weakened due to the compositional complexity of the alloy [9,10], and favorable mechanical behavior can from dislocation synergistic evolution, which contributes to effective material strengthening [11,12].

Of special note among these, is the dual phase FeMnCoCr system, which was compositionally tuned to exhibit the transformation induced plasticity (TRIP) and twinning induced plasticity (TWIP) effects, when subjected to external loading [13]. In this HEA, the TRIP effect arises from stress-assisted phase transformation, while the TWIP effect is associated with the formation of deformation twins, both of which contribute to enhanced strain hardening and ductility [14]. These deformation mechanisms are particularly sensitive to changes in phase stability, stacking fault energy and microstructural heterogeneity, all of which may be significantly altered during welding. Consequently, the presence of TRIP and TWIP effects is expected to play an important role in governing the microstructural evolution and mechanical performance of the welded joints.

On this regard, the FeMnCoCr HEA is continuously being researched in terms of understanding its microstructure and mechanical behavior [14–16]. However, beyond such investigations, the processability of such materials is a topic that requires dedicated research to avoid premature failure during its working life span. For this reason, elucidating the relationship between microstructural evolution and local compositional variations is therefore essential for accurately interpreting processing–structure–property correlations and for advancing ongoing research on these advanced alloys. Moreover, understanding the phase stability of FeMnCoCr high-entropy alloys under non-equilibrium thermal cycles, such as those experienced during welding, is essential to control precipitation behavior and microstructural degradation, thereby directly affecting weldability and corrosion resistance [17,18]

As such, amongst several processing methods that deserve attention, Gas Tungsten Arc Welding (GTAW) is a common low-cost industrial option that can be used to achieve single components out of multiple parts [19]. Moreover, of special interest is dissimilar welding, where different materials are joined permanently to perform functionally and/or structurally, depending on specific task requirements. Recently, the literature has been showcasing some systematic investigations on dissimilar welding between HEAs and conventional materials, namely Stainless Steels and Ni-superalloys [20–24]. However, to date studies specifically addressing the dissimilar welding of FeMnCoCr HEA with functional materials, such as shape memory alloys, are practically non-existent. As such, several critical topics on the compatibility of such advanced alloys remain unresolved. For instance, the interfacial microstructural evolution and phase stability in joints between HEAs and SMA are not well understood, particularly under the complex thermal cycles associated with fusion welding. Consequently, the possibility for developing optimized welding strategies and parameter windows that can simultaneously ensure joint integrity and retention of SMA functionality are still lacking.

Therefore, despite the rapid development of HEA welding research [25,26], the dissimilar welding between FeMnCoCr HEAs and SMAs remains an underexplored area, where addressing these gaps is essential. Such will allow only for understanding the fundamental interfacial mechanisms between HEAs and SMA joints, while also enabling the integration of structural HEAs with functional SMAs in advanced engineering applications.

In light of this, dissimilar welding of the dual-phase FeMnCoCr HEA with a Fe-based shape memory alloy (SMA) is conducted in the present study. Our purpose is to provide innovative and necessary data for the integration of exceptional mechanical behavior from the HEA with the recoverable deformation and functional properties of the SMA, thus opening pathways for multifunctional, high-performance structural components. Of special interest for engineering, the Fe-based SMA can be produced with similar methods as conventional steels [27–30], while showcasing the unique ability to return to its original shape when exposed to an external source of heat, after prior deformation [31].

Moreover, granted that welded joints can represent a competitive solution for structural and functional applications, it is essential to understand how welding thermal cycles influence material performance. In dual-phase high-entropy alloys, mechanical properties are strongly governed by microstructural features such as phase distribution and precipitate formation, which are highly sensitive to thermal history [32–34]. Similar sensitivities are observed in shape memory alloys (SMAs), where thermally driven microstructural evolution controls both functional and mechanical behavior [35,36]. Therefore, controlling the microstructures developed during welding is critical for tailoring the properties of both HEAs and SMAs.

As such, while autogenous welding has already been conducted in both materials [37,38], this approach envisages to infer on the behavior of a joint that comprises these two advanced materials, each exhibiting a specific set of properties.

In this study, we assess the effect of processing conditions on the microstructure using optical and scanning/transmission electron microscopy, atom probe tomography and synchrotron X-ray diffraction, further complemented by evaluation of the joint's mechanical performance via microhardness mapping and tensile testing coupled with digital image correlation. The CalPhaD method was employed to infer on the solidification path and to provide insights into the non-equilibrium solidification conditions experienced by this dissimilar material combination during welding.

Our work aims to offer an in-depth analysis of the dissimilar welding compatibility between the FeMnCoCr HEA system and the Fe-based SMA, implying the possibility of introducing HEAs in modern day engineering applications given the excellent mechanical response exhibited by the joint.

2. Materials and methods

In this work, 30 × 30 mm plates (with a thickness of 1.5 mm) of an as-rolled Fe-Mn-Si-Cr-Ni SMAs were gas tungsten arc welded (GTAW) to an FeMnCoCr HEA system, in the as-cast condition. The welding parameters were comprised of current intensity of 68 A and a torch speed of 2.5 mm/s, which was set at constant electrode-to-sample distance of 1.5 mm. These parameters were adapted from our previous work on autogenous welding conducted on the HEA [37] and on the SMA [39] and subsequently verified through preliminary dissimilar optimization welding trials to ensure stable molten pool formation and visually defect-free joints. Although heat transfer and elemental diffusion differ in dissimilar systems, the comparable melting temperature ranges and the experimentally confirmed weld quality justify the applicability of this parameter set. To avoid any welding defects and possible corrosion due to the high temperatures attained during the process the plates were cleaned with acetone and commercially pure Argon (99.999 % purity) was applied as shielding gas with a flow of 16 and 6 L/min on the face and root of the weld, respectively. Prior to welding, both materials were cleaned with acetone.

The microstructure evolution induced by the welding thermal cycle was accessed through conventional and advanced metallographic techniques. Such was possible by obtaining the cross section of the joint through electric discharge machining and subsequently following polishing procedure required to obtain a smooth and mirrored surface. Subsequently, analysis via scanning electron microscopy (SEM) imaging and electron backscatter diffraction (EBSD) were performed using a FEI Nova NanoSEM 230 equipped with an EDAX Hikari Super EBSD detector.

For optical microscopy, due to the dissimilar nature of the weld, the samples were etched with two different etching reagents, namely Nital (composed of 2.5 ml of nitric acid to 7.5 ml of hydrochloric acid) and Kaling's no. 2 (comprising 2 g of $CuCl_2$, 40 ml hydrochloric and 80 ml of ethanol). A Leica DMI5000 M inverted microscope was utilized.

Synchrotron X-ray diffraction was performed at the P07B beamline

in DESY (Germany), at Petra III. A line of consecutive scans, with a 200 μm spacing between each other, was performed throughout the full extension of the joint, working at transmission mode, utilizing a high energy X-ray beam with a wavelength of 0.14235 Å and a beam spot size of 200 × 200 μm for 0.7 s.

For further advanced nanoscale characterization and to subsequently infer on the phases that are present in the fusion zone (FZ), atom probe tomography (APT) tips and transmission electron microscopy (TEM) specimens were retrieved from three regions of interest of the FZ, depending on their distance to each of the BMs, utilizing focused ion beam (FIB) on a FEI Strata dual-beam system. The parameters for the APT analyses were set to a temperature of 50 K, and a laser pulse energy of 50 pJ at 100 kHz, while the TEM was operating at 300 kV on a Thermofisher Scientific Themis Z double-corrected microscope.

Additionally, thermodynamic calculations based on the CalPhaD method were performed using ThermoCalc software equipped with TCHEA 5.1 HEA database to predict the solidification path experienced by the molten pool.

To further access the mechanical properties exhibited by the joint a microhardness map was performed in a Mitutoyo Micro Hardness Testing Machine HM-112, with a load of 0.3 kg and dwell time of 10 s. Tensile testing, performed perpendicularly to the welding direction at a displacement rate of 1 mm/min, was conducted on an autograph Shimadzu AG50kNG machine. Simultaneously, digital image correlation (DIC) was recorded with eventual fractography being conducted in a HITACHI SU8000 SEM. The dimensions of the tensile samples are available in Fig. 1 alongside with the loading direction. Three samples of each BM and welded joint were tested to ensure reliable data and statistics.

3. Results and discussion

3.1. Microstructural analysis and microhardness distribution

An overview of the microstructural features and their influence on microhardness distribution of the joint is shown in Fig. 2. Starting from an overall perspective of the joint (refer to the microhardness map in Fig. 2(c)) and setting the center of the joint at the fusion zone (FZ), it is possible to observe the very different condition in each side, either one closer to each base material (BM), the SMA and the HEA. While the SMA BM comprises an averaged microhardness of 297 ± 11 $HV_{300\ g}$ the HEA BM is characterized by microhardness values ranging 202 ± 6 $HV_{300\ g}$. Such occurs as a direct result of composition and processing methodology carried to obtain each of the BMs, which resulted on the materials already discussed in [14,37,39], respectively. The SMA being characterized by single-phase (γ-FCC) equiaxed austenitic grains (with an average grain size of 11.4 ± 3.0 μm) comprising annealing twins, while the HEA is composed of equiaxed austenitic grains (γ-FCC), with dimensions ranging 40.2 ± 10.7 μm, with martensitic (ε-HCP) lathes in their midst.

Furthermore, moving from the BM with increasing proximity to the FZ, the heat affected zone (HAZ) becomes apparent in each side of the joint. Measurements indicated ≈ 2.5 mm on the SMA side and ≈ 2.9 mm on the HEA side, which account for the different thermal conductivity exhibited by both alloys. The microstructural complexity of this region increases due to its proximity to the molten pool during the welding process, thus being characterized by solid state transformations granted by the high temperatures experienced in the area. The high temperatures (not being sufficient to melt the material) result in the recrystallization and grain growth mechanisms that can be observed in Fig. 2(d) and (e) in the SMA side and Fig. 2(f) and (g) in the HEA.

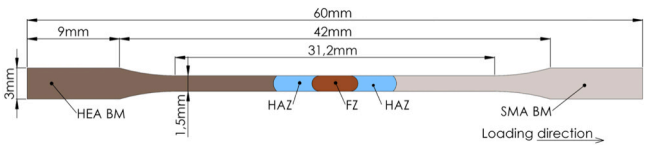

Fig. 1. Tensile samples diagram.

Between these mechanisms, grain growth is especially evident near to the FZ, while recrystallization tends to develop in HAZ closer to the BM, due to the relatively lower (albeit still high) temperatures attained further from the FZ. Such phenomenon leads to the formation of comparatively strain free grains within a solid-state matrix. Within the present case, such a region cannot be easily perceived in the microstructure when compared to both BMs. Nevertheless, an evident distinction within the HAZ in the microhardness map of Fig. 2 makes its clearly visible in the SMA side, while the microstructural differences of the HEA side are highlighted in Fig. 2(f).

Closer to the FZ, it is also possible to observe the grain growth phenomenon which occurs at higher temperatures (omitting the variable of time, which is sensibly the same for the whole extension of the HAZ during the welding). As such, it is possible to observe that both sides experienced this phenomenon, which translates in an average microhardness of 233 ± 14 $HV_{300\ g}$ in the SMA side (with an extension ranging from approximately ≈1.2 mm) and 232 ± 9 $HV_{300\ g}$ in the HEA (over an extent of ≈1.5 mm). Interestingly, in the SMA side of the joint, a partially melted zone (PMZ) can be observed at the frontier of the HAZ and the FZ, where grains were partially molten at their boundaries, leaving striations of solid metal amidst the grains of this area, such can be seen in Fig. 2(f).

Finally, we reach the FZ, at the center of the welded joint, exhibiting approximately 5.8 mm of length. This region underwent complete fusion and, in the present case, can be divided in two areas, as perceived in Fig. 2(a), (b) and (c). That is, on the SMA side of the joint the grains tend to be equiaxial dendritic, with an average size of ≈ 90.5 μm, while large and elongated grains can be found on the HEA side of the joint, exhibiting approximately ≈ 1.8 mm, measured longitudinally using the line intercept method. Such variation in the microstructure arises from the different growth rate and thermal gradient parameters depending on the proximity to each side of the joint [40].

Looking into the EBSD inverse pole figure (IPF) of Fig. 2(b), it is also possible to observe two major phenomena which occurred during solidification, these being epitaxial and competitive growth. The first can be clearly observed at the fusion boundary of the SMA side of the FZ. Upon the start of solidification, all grains grew from those already present in the BM. The second, however, can be clearly noticed at the HEA side of the joint on the EBSD IPF map, where the grains that grew aligned with the easy growth direction of the crystal structure in question (in the present case FCC, whose easy growth direction is <001 > [41]) tend to achieve lager dimensions, at the expense of grains align in other directions.

Additional compositional analysis revealed that the FZ is homogenous throughout its whole extension. However, microhardness measurements on the joint reveal that an average of 206 ± 7 $HV_{300\ g}$ can be found within the FZ region.

Further analyses were executed for three regions of the FZ, with two being chosen with attention to the proximity to each BM and the third being located at the center of the joint. Such regions were inspected via TEM and APT, with the most significant results being exposed in Fig. 3. Although highly localized, such analysis provides valuable and insightful information on the nanoscale characteristics of the joint. From this data, a clear indication of the presence of two crystal structures (γ-FCC and ε-HCP) in the FZ can be identified, as shown in Fig. 3(a), where the atomic arrangements highlight two martensitic lathes (with and HCP structure) being separated by the matrix, which is composed of FCC crystal structure. Additionally, a representative selected area electron diffraction (SAED) pattern showcased the identifiable phases as FCC and HCP with the corresponding lattice parameters as a = 3.72 Å and a = 2.61 Å, c = 4.24 Å, respectively. Furthermore, APT tips gathered from the same analyzed regions, revealed that a homogeneous distribution of the elements that compose the matrix of the joint was

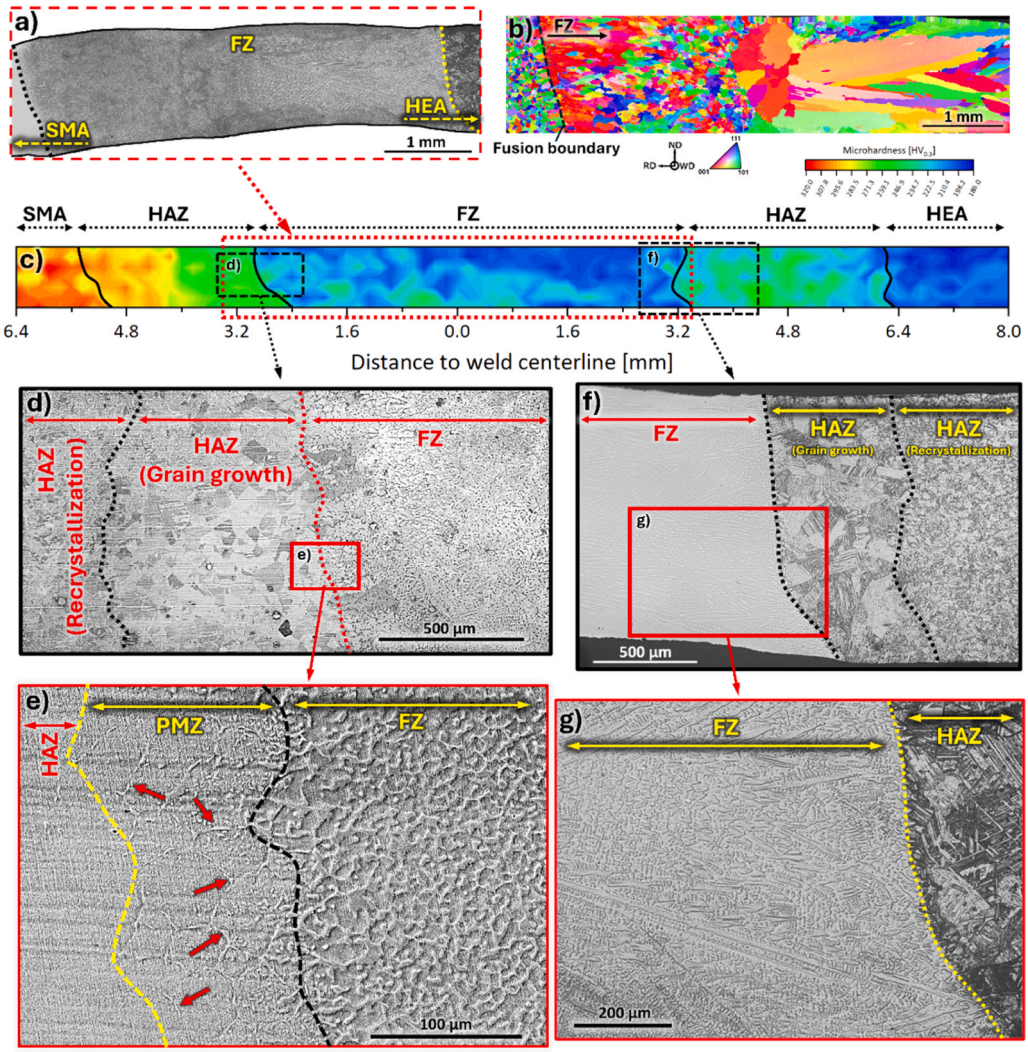

Fig. 2. Microstructural features and their influence in microhardness on the joint: (a) Optical microscopy of the welded joint and (b) EBSD IPF of the FZ highlighting grain orientation; (c) microhardness distribution across the full extension of the joint and detailed view of the HAZ close to the (d) SMA and (f) the HEA BMs. Closer attention to the transition from the HAZ to the FZ can be seen in (e) and (g) for the SMA and the HEA sides of the joint, respectively.

achieved during welding (see Fig. 3(h)), which is coherent with the solid solution effect characteristic of HEAs [42]. In line with this, EDS analysis performed across an extended area of the FZ revealed an homogenous distribution of all elements with an averaged composition of 56.3 % of Fe, 21 % of Mn, 10 % of Cr, 4.9 % of Co, 2.3 % of Ni and 5.5 % of Si (all values in at%).

In addition to this, provided that the SMA BM has VC inclusions, that are effective in improving its mechanical performance [31,43], it is also possible to observe that the high temperatures achieved in the molten pool were not sufficient for their fusion, although partial melting possibly occurred. Such precipitates can be seen in Fig. 3(b) alongside their corresponding composition maps in Fig. 3(c) and (d), thus showcasing their existence within the FZ.

Given the transformative nature of both BMs utilized to achieve this dissimilar joint, understanding the microstructure present within the joint reveals itself to be a challenging process. That is, although the formation of γ-FCC and ε-HCP phases on the HEA is to be expected and the current literature provides knowledge that the solidification path experienced by the SMA is L (Liquid) → L + γ-FCC → γ-FCC [39], the solidification path of the FZ remains unknown.

As such, the solidification path undertaken during the solidification of the molten pool was analyzed utilizing the CalPhaD methodology coupled with the previous knowledge of the data discussed so far. Here, ordered FCC and BCC phases were deselected from the database for sturdier results. Given the presence of Vanadium carbides in the FZ, the V and C content was also neglected. The results are displayed in Fig. 4.

The equilibrium results indicate that an γ-phase is generated alongside a BCC, where the γ-FCC is the matrix. However, with further solidification the amount of BCC tends to decrease with increasing γ-FCC content, until reaching ≈ 1080°C, where the nucleation of the σ phase occurs. These results are in line with the those discussed up to now, disregarding the HCP phase whose formation arises from the coalescence of stacking faults upon solidification of the molten pool [37].

3.2. Synchrotron x-ray diffraction

Although such advanced analysis techniques can grant extensive knowledge on the condition of the FZ, a more holistic approach using synchrotron x-ray diffraction was carried out to inspect the crystal structures over a wider area, over the full thickness of the joint (thus, not being secluded to surface features). Such can be observed in Fig. 5 in a complete map of the joint, produced by iterating throughout the full extension of the joint. It is displayed in terms of intensity and interplanar spacing (calculated using Bragg's law of diffraction [44]) showcased by the diffraction peak (2 0 0) of the γ-FCC phase. The (2 0 0) peak was selected due to the fact that it is the crystallographic equivalent of the

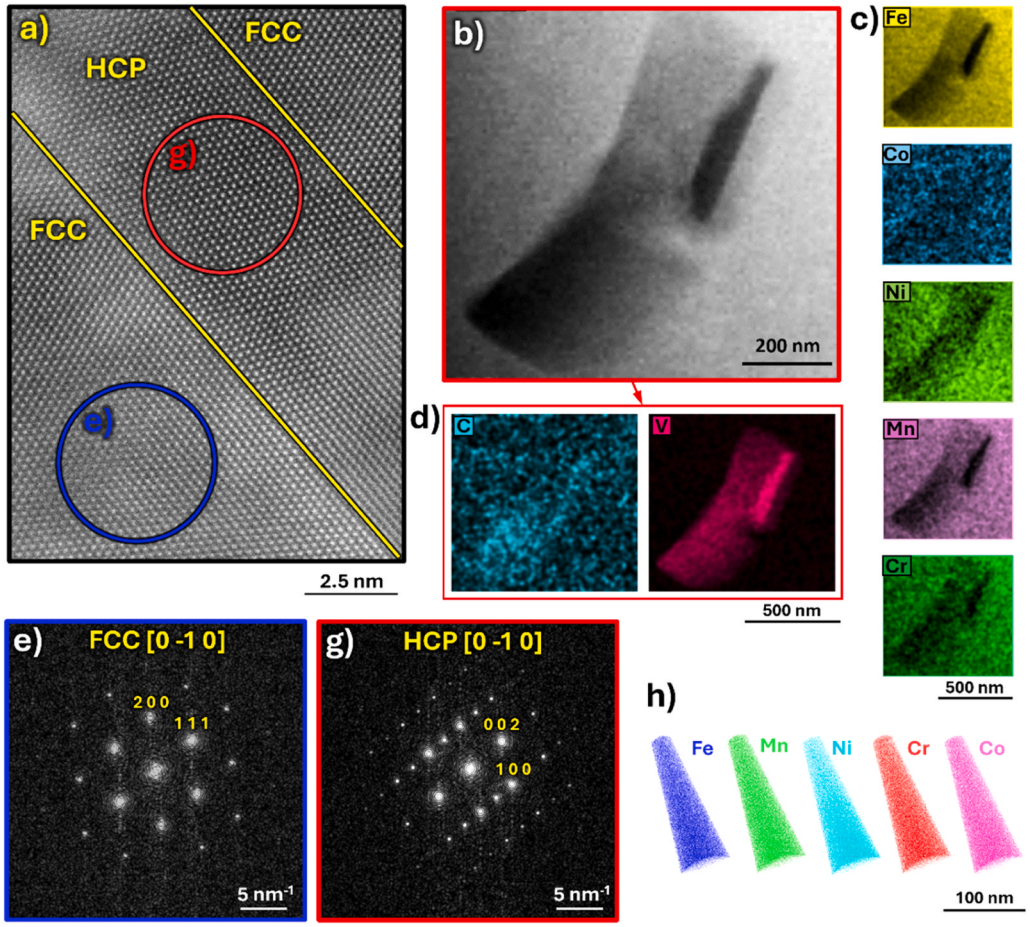

Fig. 3. Advanced characterization of the FZ using TEM and APT: (a) atomic arrangements corresponding to γ-FCC and ε-HCP phases; (b) VC precipitate and its corresponding composition maps in (c) and (d); (e) and (g) SAED pattern corresponding to the FCC and HCP phases, respectively; (h) APT tips revealing compositional homogeneity within the FZ.

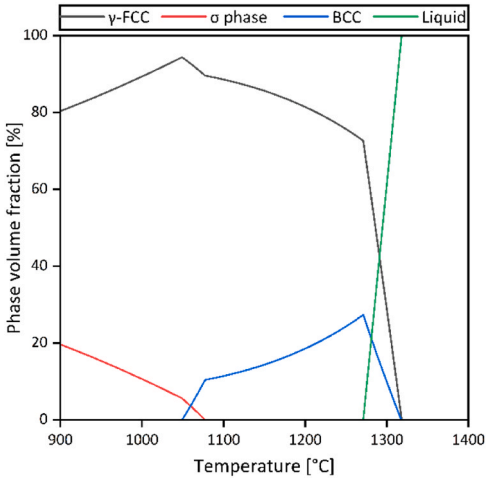

Fig. 4. One axis phase diagram depicting the solidification of FZ.

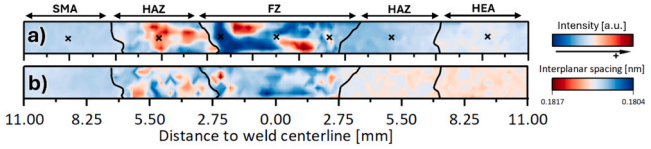

Fig. 5. Synchrotron x-ray diffraction throughout the welded joint: (a) Intensity distribution map of the (2 0 0) peak and (b) Interplanar spacing map. The diffraction patterns taken from the regions marked in (a) correspond to those presented in Fig. 6 and Fig. 7.

$< 0\ 0\ 1 >$ direction and is distanced from the influence of other diffraction peaks.

Overall, qualitatively analyzing the intensity distribution, reveals the different regions of the welded joint, however, a more quantitative inspection of the joint showcase the interplanar spacing in each of these regions. There, the higher values were achieved on the HAZ of the SMA side and the lower on the FZ (with exception to individual points). Interestingly, the HEA BM is characterized by a larger interplanar spacing than the SMA BM, which can be attributed to the different processing conditions that each BM was exposed to, alongside with their compositional differences.

Furthermore, a closer inspection of specific diffraction patterns each BM and corresponding HAZs is displayed in Fig. 6(a), (b), (c) and (e). There, smaller intensity peaks corresponding to second harmonic reflections are disregarded as marked in Fig. 7. As such, it is possible to observe that the SMA BM is composed of a γ-FCC matrix and VC precipitates, which is expected. Furthermore, the presence of the γ-FCC and ε-HCP phase is also evidenced in the HEA BM, where MnO can be also observed.

However, observing each HAZ it can be seen that different phases arose due to the high temperatures. For instances, the SMA HAZ beyond being composed of γ-FCC matrix and VC particles, the formation of ferrite (δ) can also be noted, indicating that recrystallization and grain

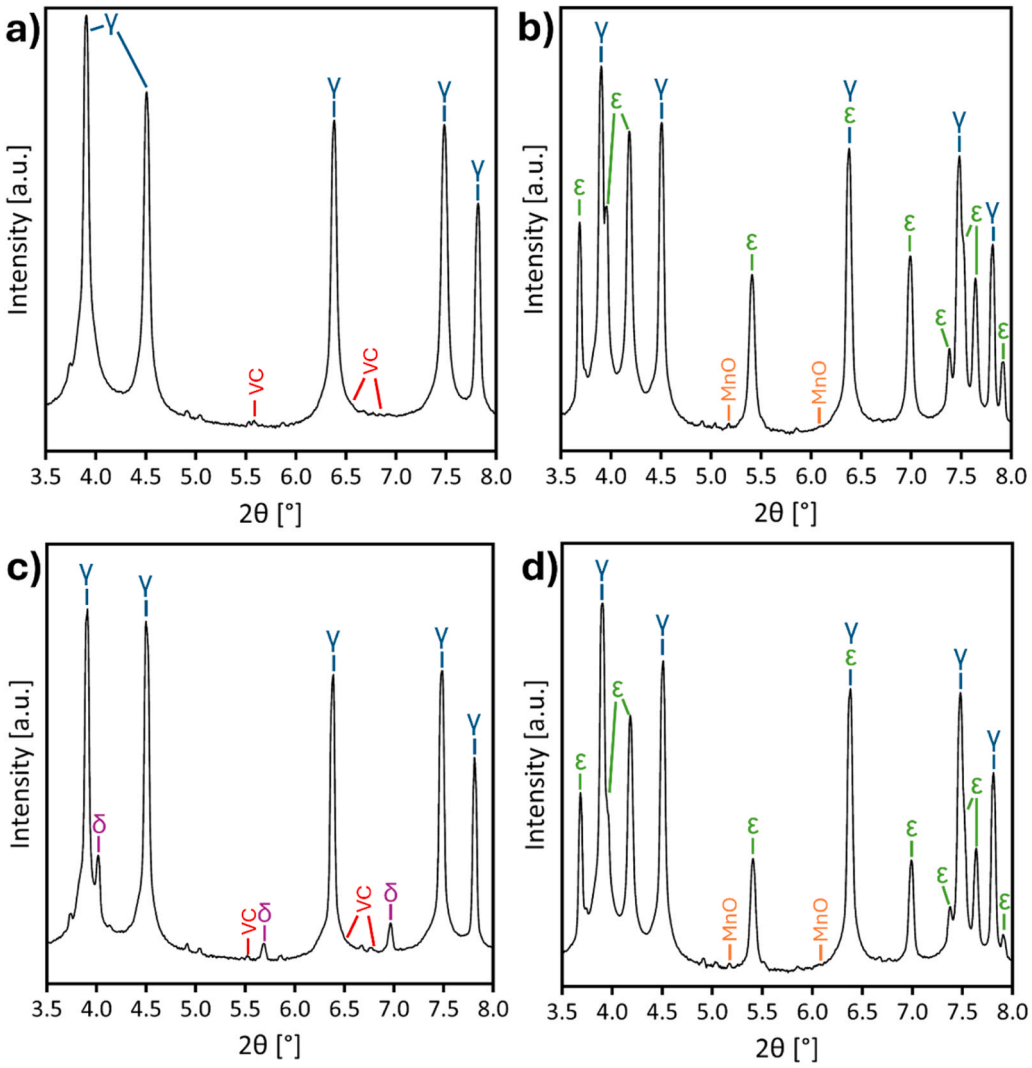

Fig. 6. Representative diffraction patterns from the (a) the SMA BM, (b) the HEA BM, (c) the HAZ from the SMA side and (d) the HAZ from the HEA side of the joint.

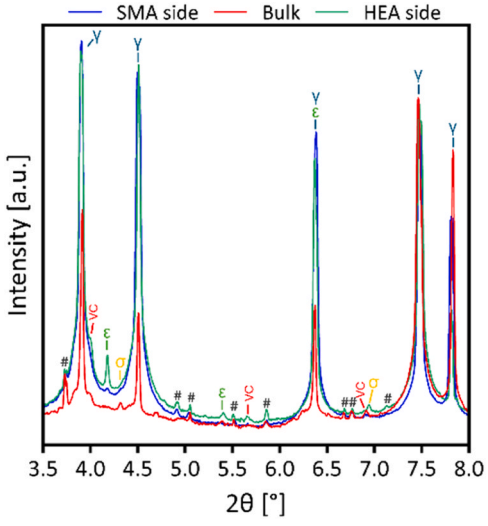

Fig. 7. Superimposition of the diffraction pattern taken from the FZ, namely closer to each of the BMs and at its bulk.

growth are not the only phenomena occurring within this region. Nevertheless, on the other side of the joint, the HAZ exhibits the same phases as those seen in the HEA BM, as expected from [37].

Moreover, quantitative analysis, gathered via Rietveld refinement, using MAUD software [45], revealed for the HEA BM an approximate volume fraction of 33 % for γ-FCC, with the remaining 67 % corresponding to the ε-HCP phase and with the MnO being practically unnoticeable. The SMA BM, however, showcased an overall phase volume fraction of 99 % corresponding to the γ-FCC, with the remaining 1 % is related to the VC precipitates. Furthermore, analyzing the HAZ on the HEA side, the data revealed and increase on the phase volume fraction of the γ-FCC phase up to nearly 80 %. Within the HAZ on the SMA side, the γ-FCC phase constitutes approximately 96 vol%, while the δ phase accounts for about 3 %, and the remaining 1 % corresponds to the VC precipitates.

Furthermore, observing representative diffraction patterns within the FZ, its bulk and close to each side, it can be seen that over its full extent it is composed by a amalgamation of all the phases present in each of the BMs, with exception to δ and MnO. Interestingly, small intensity peaks corresponding to sigma phase (σ) were also encountered.

Similarly to the BM and HAZs, further analysis using Rietveld refinement was conducted on these three analyzed regions of the FZ, in which case the amount of σ was disregarded due to its very low content (less than 0.2 %). The results showcased a decreasing gradient in VC precipitates volume fraction with increasing distance to the SMA side of

the joint, with a volume fraction of ≈ 0.9 % close to the SMA HAZ, ≈ 0.5 % in the bulk of the FZ and 0.4 % near the HEA HAZ. Additionally, the amount of γ-FCC and ε-HCP varies within the range of 97–98 % throughout the FZ with the remaining 2–3 % corresponding to the ε-HCP phase.

Accordingly, the CalPhaD calculations predict the formation of σ phase under equilibrium conditions at high temperatures (refer to Fig. 4), assuming sufficient time for long-range diffusion and chemical homogenization. However, such phase can still nucleate due to constitutional undercooling conditions and incomplete solute redistribution in the FZ, resulting in microsegregation of σ-stabilizing elements in the interdendritic regions. These can shift the phase stability locally due to kinetic effects and diffusion limitations and, consequently, favor the formation of σ phase within the microstructure in detriment of other phases such as the matrix γ-FCC.

3.3. *Tensile testing performance*

Given that a thorough analysis of the microstructure was conducted, the next logical step is to analyze the resultant mechanical performance of the dissimilar joint via the tensile test, which yields some of the most important results in necessary for structural engineering (refer to Fig. 8). Overall, the SMA yielded a maximum tensile stress of approximately 980 MPa, with eventual fracture occurring at a strain of ≈ 37.8 %. Conversely, the HEA attained a maximum tensile stress of ≈ 725 MPa, finally fracturing at ≈ 38.9 %. The welded joint, however, managed to reach ≈ 671 MPa, at a strain of ≈ 15.5 %, upon which it fractured. DIC analysis of the mechanical behavior of the joint, indicated that FZ was the region where most of the strain was accommodated, being followed by each HAZs and BMs, where the SMA BM exhibited the least amount of strain in the joint during testing.

Upon eventual fracture at the boundary between the FZ and the HAZ of the HEA side of the weld fractography was conducted, as displayed in Fig. 9. The fracture surface exhibits predominantly ductile features, characterized by the presence of dimples, confirming this region as the critical failure location within the joint. Amidst the dimples it is also possible to observe the presence of Mn precipitates with a round shape [46] and some cleavage voids were the VC precipitates may have been located. Moreover, the fact that it occurs at the interface is attributed to its lower mechanical strength, resulting from the combined effects of mechanical mismatch and microstructural heterogeneity, which can act as stress concentrators and potential sites for void initiation. Consequently, fracture stems in this region despite the retained ductility of the FZ.

Moreover, the higher strain accommodated by the FZ, visible in Fig. 8, can be attributed to its heterogeneous phase constitution, where the metastable γ- FCC matrix may undergo strain-induced transformation to ε-HCP, consistent with TRIP/TWIP-like mechanisms reported in the FeMnCoCr HEA [14]. Additionally, the presence of the ε-HCP phase can provide an additional deformation pathway, enhancing work hardening and delaying strain localization, which contributes to the sustained ductility of the joint. Furthermore, although the σ phase is intrinsically brittle, its detrimental effect appears to be mitigated by the surrounding γ-FCC matrix, which can accommodate plastic strain through phase transformation. In addition, the presence of finely dispersed Mn oxides in the FZ may hinder dislocation motion and promote the formation dislocation forests, further enhancing work hardening. As a result, the retained ductility, despite the presence of σ, may be ascribed to the combined effects of TRIP-assisted deformation and dislocation strengthening facilitated by the complex microstructure [37, 47].

As such, the preferential fracture at the FZ and HAZ interface on the HEA side can be further rationalized by considering the correlation between local stress concentration and the interfacial microstructure. This means that the abrupt transition in phase structure, precipitate distribution and grain morphology introduces pronounced mechanical

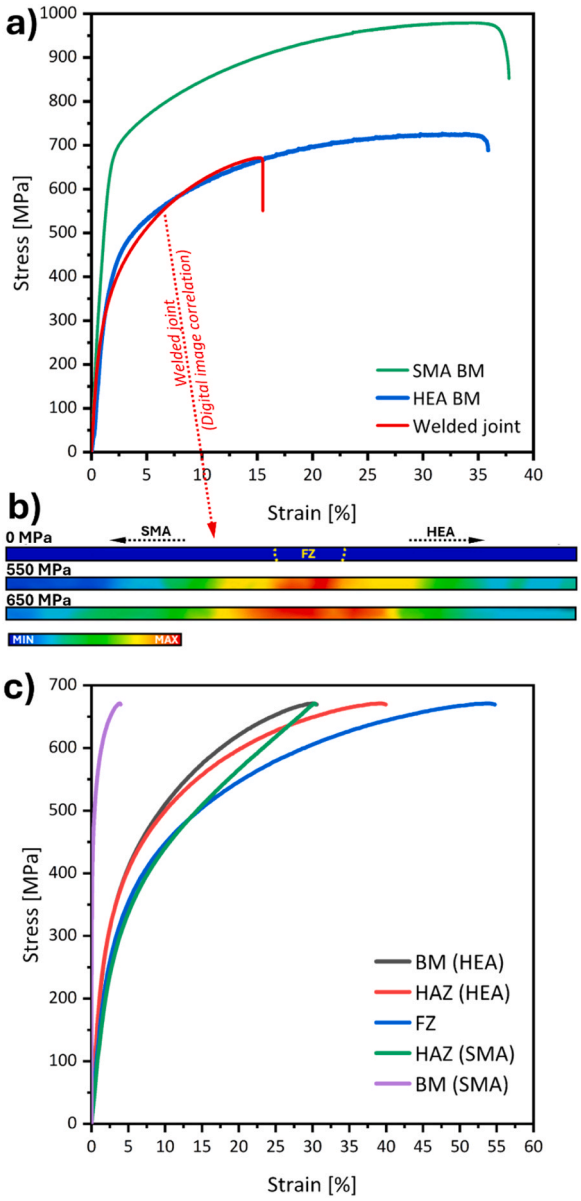

Fig. 8. (a) Representative mechanical response to tensile stress of the welded joints, the SMA and the HEA BMs; (b) DIC results showcasing local strain distribution before fracture;(c) DIC point analysis obtained during tensile testing.

heterogeneity, which leads to strain incompatibility during tensile loading. As deformation progresses, stress concentrates at grain boundaries and around second-phase particles, where differences in elastic and plastic response impede uniform strain accommodation. This facilitates crack nucleation at microstructural discontinuities, after which they tend to propagate. Consequently, as resistance to crack growth is reduced by the combined effects of microstructural heterogeneity and local mechanical behavior mismatch, this boundary between the HAZ and the FZ on the HEA side governs the fracture behavior of the joint despite the overall ductile response of the joint.

4. Conclusions

Dissimilar welding via GTAW, between an FeMnCoCr HEA and an Fe-based SMA was successfully performed. The following conclusions can be drawn.

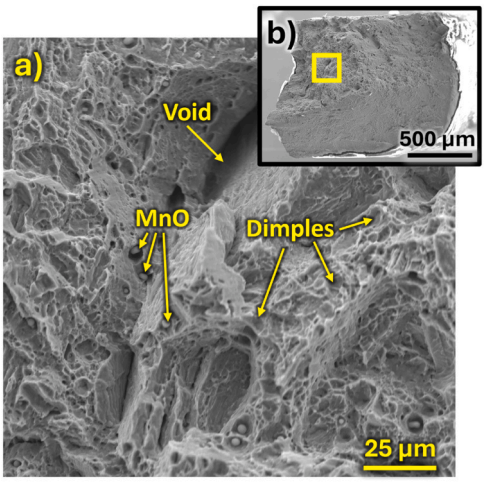

Fig. 9. Fracture surface of the gas tungsten arc welded dissimilar joint.

- No welding defects were encountered in the joints, proving a good weldability between the two materials.
- Solid state phenomena, such as recrystallization and grain growth, occurring in the HAZ of both sides of the welded joint were clearly visible, via microscopy and mechanical testing methods. Such occurred as a product of the thermal cycles developed during the welding process.
- Advanced characterization techniques, including TEM, APT and SXRD permitted to observe the phases present throughout the full extension of the FZ. Of special emphasis was the formation of the δ phase in the HAZ of the SMA side and the formation of σ phase within the FZ.
- A large discrepancy in terms of grain size within the FZ was found with regard to the proximity to each BM.
- Mechanical testing revealed that the joint could endure a maximum stress of 671 MPa before fracturing at a strain of ≈ 15.5 %. These are excellent mechanical properties for a dissimilar joint, albeit lower than the mechanical performance of each BM.

Overall, the presented result highlight to the possibility of matching HEAs and other advanced engineering alloys for modern day engineering applications.

CRediT authorship contribution statement

B. Wang: Investigation. **R.S. Mishra:** Investigation. **N. Schell:** Investigation. **T. Boll:** Methodology, Investigation, Data curation. **J. Shen:** Investigation. **B. Li:** Investigation. **D. Wang:** Investigation, Formal analysis. **Oliveira J. P.:** Writing – review & editing, Visualization, Supervision, Resources, Project administration, Investigation. **Baptista A. C.:** Investigation. **A. Alvarez:** Investigation, Formal analysis, Data curation, Conceptualization. **Lopes J G.:** Writing – review & editing, Writing – original draft, Visualization, Supervision, Methodology, Investigation, Formal analysis, Data curation, Conceptualization.

Declaration of Competing Interest

The authors declare that they have no known competing financial interests or personal relationships that could have appeared to influence the work reported in this paper.

Acknowledgments

JGL, AA, AC, JS and JPO acknowledge the funding by National Funds from FCT - Fundação para a Ciência e a Tecnologia, I.P., in the scope of the projects LA/P/0037/2020, UIDP/50025/2020 and UIDB/50025/2020 of the Associate Laboratory Institute of Nanostructures, Nanomodelling and Nanofabrication – i3N. The authors acknowledge DESY (Hamburg, Germany), a member of the Helmholtz Association HGF, for the provision of experimental facilities. Beamtime was allocated for proposal I-20231128 EC. The research leading to this result has been supported by the project CALIPSOplus under the Grant Agreement 730872 from the EU Framework Program for Research and Innovation HORIZON 2020. This project has received funding from the European Union's Horizon 2020 research and innovation program under grant agreement No 101007417, having benefited from the access provided by KIT (Germany) within the framework of the NFFA-Europe Pilot Transnational Access Activity, proposal ID161. The raw/processed data required to reproduce these findings is available, accordingly to NFFA Europe regulations.

References

[1] J.W. Yeh, Recent progress in high-entropy alloys, Annales de Chimie Science Des Materiaux 31 (2006) 633–648, https://doi.org/10.3166/acsm.31.633-648.
[2] D.B. Miracle, O.N. Senkov, A critical review of high entropy alloys and related concepts, Acta Mater. 122 (2017) 448–511, https://doi.org/10.1016/j.actamat.2016.08.081.
[3] D.D.S. Silva, G. Bertoli, N.D.C. Neto, N. Schell, K.D. Clarke, M.J. Kaufman, A. J. Clarke, F.G. Coury, C. Bolfarini, Computational thermodynamics-guided alloy design and phase stability in CoCrFeMnNi-based medium-and high-entropy alloys: an experimental-theoretical study, Scr. Mater. 252 (2024) 116264, https://doi.org/10.1016/J.SCRIPTAMAT.2024.116264.
[4] K. Khanchych, C. Tang, C. Schroer, B. Schäfer, J. Jung, M. Dürrschnabel, U. Jäntsch, B. Gorr, CALPHAD-guided prediction and interpretation of phase formation in Ta–Mo–Cr–Ti–Al refractory high-entropy alloys, Adv. Eng. Mater. (2025) 2500527, https://doi.org/10.1002/ADEM.202500527;REQUESTEDJOURNAL:JOURNAL:15272648;PAGE:STRING:ARTICLE/CHAPTER.
[5] J. Han, N. Lei, D. Zhou, S. Long, Z. Yu, Y. Yi, Doping B or C to improve the wear resistance of (Ti42.5Zr42.5Nb10Ta5)93Mo7 refractory high-entropy alloy via grain boundary plasticization, Wear (2026) 584–585, https://doi.org/10.1016/J.WEAR.2025.206385.
[6] Q. Zhou, Z. Jiao, Z. Huang, Y. Shi, Y. Li, C. Yin, H. Wang, H.C. Pinto, C. Greiner, W. Liu, Wear-resistant CrCoNi nanocrystalline film via friction-driven surface segregation, Acta Mater. 279 (2024) 120299, https://doi.org/10.1016/J.ACTAMAT.2024.120299.
[7] L.L. Zhang, X.S. Wei, M. Shahbaz, Z.Z. Jiang, T.C. Ma, J.B. Pang, J. Shen, Accelerated discovery of corrosion resistant FeWTiTaB refractory high-entropy amorphous alloys in liquid lead-bismuth eutectic, Corros. Sci. 260 (2026) 113515, https://doi.org/10.1016/J.CORSCI.2025.113515.
[8] Z. Yuan, Z. Yang, M. Jiang, L. Huang, Y. Tu, T. Yuan, Z. Ni, F. Liu, X. Chen, X. Wang, Investigation of the effect of Al content on the microstructure and corrosion behavior of as-cast AlxCoCrFeNi high-entropy alloys, Corros. Sci. 259 (2026) 113510, https://doi.org/10.1016/J.CORSCI.2025.113510.
[9] Y. Li, X. Wang, A. Lan, J. Qiao, Helium ion irradiation-induced hardening behavior in Ti1.5ZrHf0.5Nb0.5Ta0.5 refractory high-entropy alloys, J. Nucl. Mater. 616 (2025) 156037, https://doi.org/10.1016/J.JNUCMAT.2025.156037.
[10] C. Xu, P. Li, X. Tian, W. Jiang, Q. Wang, H. Fan, Irradiation-induced grain boundary strengthening/embrittlement in bcc refractory high entropy alloy TiZrHfNbTa, J. Nucl. Mater. 617 (2025) 156163, https://doi.org/10.1016/J.JNUCMAT.2025.156163.
[11] P. Ma, H. Wang, H. Zhang, Y. Lin, Z. Zhang, X. Zhang, R. Chen, The mechanism of multi-component dislocation synergistic evolution and material strengthening in the as-cast TiZrNbV refractory high-entropy alloy, Int. J. Plast. 195 (2025) 104505, https://doi.org/10.1016/J.IJPLAS.2025.104505.
[12] R. Wang, Y. Fan, R. Chen, Y. Fang, Y. Chen, P. Wang, H. Wang, Y. Tang, S. Bai, Enhancing strain hardening and strength-plasticity synergy upon dynamic loads in refractory high-entropy alloys via B2 ordering and spinodal decomposition, Int. J. Plast. 194 (2025) 104482, https://doi.org/10.1016/J.IJPLAS.2025.104482.
[13] Z. Li, C.C. Tasan, K.G. Pradeep, D. Raabe, A TRIP-assisted dual-phase high-entropy alloy: grain size and phase fraction effects on deformation behavior, Acta Mater. 131 (2017) 323–335, https://doi.org/10.1016/J.ACTAMAT.2017.03.069.
[14] J.G. Lopes, J. Shen, E. Maawad, P. Agrawal, N. Schell, R.S. Mishra, J.P. Oliveira, Time-resolved evolution of the deformation mechanisms in a TRIP/TWIP Fe50Mn30Co10Cr10 high entropy during tensile loading probed with synchrotron X-ray diffraction, Int. J. Plast. 179 (2024) 104048, https://doi.org/10.1016/J.IJPLAS.2024.104048.
[15] N. Ali, L. Zhang, L. Dongming, H. Zhou, K. Sanaullah, C. Zhang, Y. Nian, J. Cheng, Enhancing the strength-ductility synergy in hot-forged Fe50Mn30Co10Cr10 high entropy alloy (HEA) through carbon additions, J. Mater. Res. Technol. 29 (2024) 5646–5655, https://doi.org/10.1016/J.JMRT.2024.02.232.
[16] X.F. Wang, Z.P. Wang, Y.L. Bian, Y. Cai, N.B. Zhang, L. Lu, S.N. Luo, Improving ductility and strength of high-entropy alloy Fe50Mn30Co10Cr10 via multi-directional forging and annealing, Mater. Sci. Eng. A 915 (2024) 147258, https://doi.org/10.1016/J.MSEA.2024.147258.

[17] H. Sharma, B. Rajput, R.P. Singh, A review paper on effect of input welding process parameters on structure and properties of weld in submerged arc welding process, Mater. Today Proc. 26 (2020) 1931–1935, https://doi.org/10.1016/J.MATPR.2020.02.422.
[18] Y. Ma, Z. Jiao, Z. Huang, Q. Zhou, T. Huang, X. Ran, Z. Wang, L. Qiu, H. Teng, X. Lu, Z. Shen, H. Wang, Exploration on the oxidation resistance of TiAlNbN films: mechanisms of nanopore regulation and crack suppression, Corros. Sci. 257 (2025) 113273, https://doi.org/10.1016/J.CORSCI.2025.113273.
[19] Q. Guo, Z. Yang, J. Xu, Y. Jiang, W. Wang, Z. Liu, W. Zhao, Y. Sun, Progress, challenges and trends on vision sensing technologies in automatic/intelligent robotic welding: state-of-the-art review, Robot. Comput. Integr. Manuf. 89 (2024) 102767, https://doi.org/10.1016/J.RCIM.2024.102767.
[20] M. Rhode, K. Erxleben, T. Richter, D. Schroepfer, T. Mente, T. Michael, Local mechanical properties of dissimilar metal TIG welded joints of CoCrFeMnNi high entropy alloy and AISI 304 austenitic steel, 2024 68:6, Weld. World 68 (2024) 1563–1573, https://doi.org/10.1007/S40194-024-01718-4.
[21] R. Sokkalingam, B. Pravallika, K. Sivaprasad, V. Muthupandi, K.G. Prashanth, Dissimilar welding of high-entropy alloy to Inconel 718 superalloy for structural applications, 2021 37:1, J. Mater. Res. 37 (2021) 272–283, https://doi.org/10.1557/S43578-021-00352-W.
[22] H. Peng, S. Huang, L. Hu, I. Baker, Dissimilar electron beam welding of the medium-entropy alloy Ni43.4Co25.3Cr25.3Al3Ti3 and 316 stainless steel for cryogenic application, Intermetalics 175 (2024) 108546, https://doi.org/10.1016/J.INTERMET.2024.108546.
[23] R. Sokkalingam, B. Pravallika, K. Sivaprasad, V. Muthupandi, K.G. Prashanth, Dissimilar welding of high-entropy alloy to Inconel 718 superalloy for structural applications, 2021 37:1, J. Mater. Res. 37 (2021) 272–283, https://doi.org/10.1557/S43578-021-00352-W.
[24] N.K. Adomako, G. Shin, N. Park, K. Park, J.H. Kim, Laser dissimilar welding of CoCrFeMnNi-high entropy alloy and duplex stainless steel, J. Mater. Sci. Technol. 85 (2021) 95–105, https://doi.org/10.1016/J.JMST.2021.02.003.
[25] J.Q. Tang, J. Li, K. Liu, C. Xu, T. Sonar, Weldability and welding technology of high-entropy alloys: a review, 2025 32:4, J. Cent. South Univ. 32 (2025) 1141–1166, https://doi.org/10.1007/S11771-025-5949-8.
[26] J.G. Lopes, J.P. Oliveira, A short review on welding and joining of high entropy alloys, Metals 10 (2020) 212, https://doi.org/10.3390/met10020212.
[27] C. Czaderski, M. Shahverdi, J. Michels, Iron based shape memory alloys as shear reinforcement for bridge girders, 2021. https://doi.org/10.1016/j.conbuildmat.2020.121793.
[28] A.V. Druker, A. Perotti, I. Esquivel, J. Malarría, A manufacturing process for shaft and pipe couplings of Fe-Mn-Si-Ni-Cr shape memory alloys, 2013. https://doi.org/10.1016/j.matdes.2013.11.032.
[29] I. Ferretto, D. Kim, N.M. Della Ventura, M. Shahverdi, W. Lee, C. Leinenbach, Laser powder bed fusion of a Fe-Mn-Si shape memory alloy, Addit. Manuf. 46 (2021) 102071, https://doi.org/10.1016/j.addma.2021.102071.
[30] J. Vůjtěch, P. Ryjáček, J. Campos Matos, E. Ghafoori, Iron-based shape memory alloy for strengthening of 113-year bridge, (2021). https://doi.org/10.1016/j.engstruct.2021.113231.
[31] A. Cladera, B. Weber, C. Leinenbach, C. Czaderski, M. Shahverdi, M. Motavalli, Iron-based shape memory alloys for civil engineering structures: an overview, Constr. Build. Mater. 63 (2014) 281–293, https://doi.org/10.1016/J.CONBUILDMAT.2014.04.032.
[32] B. Luan, J. Gao, P. Wang, J. Cheng, Y. He, M. He, Subgrain boundary-driven spheroidization synergistically enhances strength and ductility in Ni-based eutectic medium-entropy alloys, Scr. Mater. 274 (2026) 117146, https://doi.org/10.1016/J.SCRIPTAMAT.2025.117146.
[33] B. Luan, J. Gao, F. Jiang, P. Wang, J. Cheng, Y. He, M. He, Research progress on the mechanical properties of eutectic high-entropy alloys, J. Alloy. Compd. 1050 (2026) 185642, https://doi.org/10.1016/J.JALLCOM.2025.185642.
[34] Y. ling Gu, M. ling Yi, Y. Chen, J. Tu, Z. ming Zhou, J. ru Luo, Effect of the amount of SiC particles on the microstructure, mechanical and wear properties of FeMnCoCr high entropy alloy composites, Mater. Charact. 193 (2022) 112300, https://doi.org/10.1016/J.MATCHAR.2022.112300.
[35] B.C. Maji, M. Krishnan, Gouthama, R.K. Ray, Role of Si in improving the shape recovery of FeMnSiCrNi shape memory alloys, Metall. Mater. Trans. A Phys. Metall. Mater. Sci. 42 (2011) 2153–2165, https://doi.org/10.1007/S11661-011-0651-X.
[36] B.C. Maji, M. Krishnan, Effect of copper addition on the microstructure and shape recovery of Fe–Mn–Si–Cr–Ni shape memory alloys, Mater. Sci. Eng. A 570 (2013) 13–26, https://doi.org/10.1016/J.MSEA.2013.01.061.
[37] J.G. Lopes, P. Agrawal, J. Shen, N. Schell, R.S. Mishra, J.P. Oliveira, Evolution of microstructure and mechanical properties in gas tungsten arc welded dual-phase Fe50Mn30Co10Cr10 high entropy alloy, Mater. Sci. Eng. A 878 (2023) 145233, https://doi.org/10.1016/J.MSEA.2023.145233.
[38] J. Shen, W. Zhang, J.G. Lopes, Y. Pei, Z. Zeng, E. Maawad, N. Schell, A.C. Baptista, R.S. Mishra, J.P. Oliveira, Evolution of microstructure and deformation mechanisms in a metastable Fe42Mn28Co10Cr15Si5 high entropy alloy: a combined in-situ synchrotron X-ray diffraction and EBSD analysis, Mater. Des. 238 (2024) 112662, https://doi.org/10.1016/j.matdes.2024.112662.
[39] J.G. Lopes, D. Martins, K. Zhang, B. Li, B. Wang, X. Wang, N. Schell, E. Ghafoori, A. C. Baptista, J.P. Oliveira, Unveiling the microstructure evolution and mechanical properties in a gas tungsten arc-welded Fe–Mn–Si–Cr–Ni shape memory alloy, J. Mater. Sci. 2024 (2024) 1–22, https://doi.org/10.1007/S10853-024-09606-4.
[40] S. Kou, Welding metallurgy, welding metallurgy 2002. https://doi.org/10.1002/0471434027.
[41] R.E. Reed-hill, Physical metallurgy PWS-KENT, 2015. ⟨https://archive.org/details/physicalmetallur0000reed⟩ (accessed February 27, 2023).
[42] J.W. Yeh, S.K. Chen, S.J. Lin, J.Y. Gan, T.S. Chin, T.T. Shun, C.H. Tsau, S.Y. Chang, Nanostructured high-entropy alloys with multiple principal elements: novel alloy design concepts and outcomes, Adv. Eng. Mater. 6 (2004) 299–303, https://doi.org/10.1002/ADEM.200300567.
[43] M. Koster, W.J. Lee, M. Schwarzenberger, C. Leinenbach, Cyclic deformation and structural fatigue behavior of an FE–Mn–Si shape memory alloy, Mater. Sci. Eng. A 637 (2015) 29–39, https://doi.org/10.1016/J.MSEA.2015.04.028.
[44] B.B. He, Two-Dimensional X-ray diffraction, two-dimensional x-ray diffraction (2009. 1–426. https://doi.org/10.1002/9780470502648.
[45] L. Lutterotti, IUCr, Maud: a Rietveld analysis program designed for the internet and experiment integration, Urn:Issn:0108-7673 56 2000. pp. 54–54. https://doi.org/10.1107/S0108767300021954.
[46] A.M. Hossain, N. Kumar, Microstructure and mechanical properties of a dual phase transformation induced plasticity Fe-Mn-Co-Cr high entropy alloy, J. Alloy. Compd. 893 (2022) 162152, https://doi.org/10.1016/J.JALLCOM.2021.162152.
[47] D. Hua, Q. Xia, W. Wang, Q. Zhou, S. Li, D. Qian, J. Shi, H. Wang, Atomistic insights into the deformation mechanism of a CoCrNi medium entropy alloy under nanoindentation, Int. J. Plast. 142 (2021) 102997, https://doi.org/10.1016/J.IJPLAS.2021.102997.